Regular Dimpled Nickel Surfaces for Improved Efficiency of the Oxygen Evolution Reaction

Audrey K. Taylor, Irene Andreu, and Byron D. Gates [*]

Prof. Byron D. Gates, Ms. Audrey K. Taylor, and Dr. Irene Andreu

Department of Chemistry

Simon Fraser University

8888 University Drive

Burnaby, BC V5A 1S6 (Canada)

Telephone Number: (778) 782-8066

Fax Number: (778) 782-3765

* Email Address: bgates@sfu.ca

Abstract

Persistent bubble accumulation during the oxygen evolution reaction (OER) can effectively block catalytically active surface sites and reduce overall system performance. The OER is an essential half reaction with relevance to metal-air batteries, fuel cells, and water electrolysis for power to gas applications. The renewable energy sector could benefit from the identification of surface morphologies that can effectively reduce the accumulation of bubbles on electrocatalytic surfaces. In this work, regular dimpled nickel (Ni) features were prepared to investigate how electrode morphology and, therefore, its roughness and wetting properties may affect the efficiency of the OER. The dimpled Ni features were prepared using spherical poly(styrene) (PS) templates with a diameter of 1 µm. The electrodeposition against regular, self-assembled arrays of PS templates was tuned to produce four types of dimpled features each with a different depth. Enhancements to the OER efficiency were observed for some types of dimpled Ni features when compared to a planar electrodeposited Ni electrode, while the dimpled features that were the most recessed demonstrated reduced efficiencies for the OER. The findings from this study emphasize the influences of electrode surface morphology on processes involving electrocatalytic gas evolution.

Introduction

The accumulation of bubbles on the surface of electrodes during the oxygen evolution reaction (OER) presents a problematic physical resistance that can become even more persistent with highly active electrodes. The identification and development of surface morphologies to assist in the evolution and removal of oxygen bubbles from electrode surfaces could enhance the efficiency of the OER. In this work, regular arrays of dimpled nickel (Ni) features were prepared to investigate how electrode morphology may affect the efficiency of the OER. The OER is a fundamental electrochemical process utilized in several clean energy technologies, such as in metal-air batteries,[1] water electrolyzers,[2] and fuel cells.[3] Improving the efficiency of the OER could increase its utility in the renewable energy sector through a reduction in the operational costs per kW. For instance, in large-scale applications of water electrolysis, the applied potential needed to drive the reaction is much higher than what is theoretically predicted (e.g., >1.23 V at 25 °C).[4] The overall efficiency of commercially available electrolysis devices remains between 59 and 70%.[5] Delayed reaction kinetics and inherent resistances, specifically at the anodic working electrode where the OER takes place, are known to cause these less than ideal efficiencies.

Recent work to improve the OER performance has focused on identifying catalyst compositions that are more active based on mixtures of first-row transition metals (e.g., Ni, Fe, Co, Mn).[6] These earth abundant metals are relatively stable in harsh, alkaline conditions and have demonstrated lower overpotentials than industrial research standards (IrO_2 and RuO_2)[7, 8] making these catalysts attractive for use in commercial devices. Relatively low overpotentials have been demonstrated for NiFe thin film catalysts.[8–10] In recent work by Zhao *et al*., mesoporous NiFe nanosheets were electroplated onto a macroporous Ni foam.[10] The authors

concluded that the observed enhancements in the OER activity were a result of the hierarchical structure. The rippled NiFe nanosheets, with a thickness of 10 nm, formed a mesoporous structure (~50 to 100 nm in length, with a separation of ~50 nm between the nanosheets), which was hypothesized to improve the wetting properties of the Ni foam as oxygen bubbles were not seen to accumulate on the electrode surfaces. Large oxygen bubbles were efficiently removed from this catalyst through the macroporous channels throughout the foam. Although the work of Zhao *et al*. highlighted the utility of accessing a morphology that contains more than one size-domain, it remains unclear if there are optimal geometric dimensions that may promote removal of oxygen bubbles from electrode surfaces. It is, however, known that roughness and wettability both influence the behavior of bubbles on electrode surfaces. For example, increasing the hydrophilicity of electrode surfaces can enhance bubble removal through more favorable interactions with the electrolyte that decrease the solid-liquid surface tension.[11, 12]

The wettability of a material can be controlled through modifications of its surface roughness. Experimental studies have shown that highly roughened or textured surfaces can demonstrate a high degree of wetting, as described by the Wenzel model.[13, 14] In the work of Ahn *et al.*, surface roughness of Ni was tuned by varying the electrodeposition potential.[12] Four types of roughened electrode surfaces were produced on Ni electrodes each with a different root mean squared (RMS) roughness. The RMS roughness was tuned ranging from ~12 nm to ~52 nm. Improved OER activity was correlated to a decrease in the solid-liquid surface tension with increasing surface roughness. The roughest surface exhibited a needle-like morphology, which was observed to release bubbles with a smaller diameter than the other types of electrodes as determined from photographs acquired during chronoamperometry (CA) measurements. Although the authors reported a smaller bubble break-off diameter and inferred a smaller bubble

overpotential for those needle-like electrodes, the investigation did not account for the differences in active surface area for each type of electrode when assessing their performance for the OER. In work by Zeng *et al.*, modifications to Ni electrodes were made by mechanical polishing with three different types of sandpaper, each with a distinct grain size or grit.[15] Roughness of the electrode surfaces was used to evaluate their efficiency for the hydrogen evolution reaction (HER). The lowest overpotentials were exhibited by Ni surfaces polished with the coarsest sandpaper (~35 µm-diameter grains), which had the highest roughness factor as estimated by impedance spectroscopy measurements. The improved performance of these electrodes for the HER was attributed to their larger active surface area. It was suggested that if the electrochemically active surface area (ECSA) of the Ni could be accurately determined the electrodes would each have similar activities. The effects of surface morphology can be difficult to discern without accounting for the true surface area. Many electrodes with a roughened surface morphology have exhibited an improved electrocatalytic activity, but very few studies have simultaneously demonstrated control over geometric surface features.[16–19] In the absence of controlling the surface geometry, it is difficult to determine with absolute certainty what the specific contributions are from each factor that influences the observed enhancement in activity. For example, the morphological effects will be difficult to distinguish from the ECSA enhancements without accurately accounting for the surface geometry of the features. Our aim here is to precisely control surface morphology of Ni electrodes by preparing features with regular dimensions that enable an assessment of the correlation between the OER activity, the surface area, and the structure of the surfaces of these electrodes.

In this work, we prepared Ni electrodes that contained regular arrays of dimpled features on their surfaces. The surface morphology of these electrodes was tuned, creating a series of

electrodes with well-defined changes in surface area and geometry. The electrochemical efficiency of each of these structured electrodes was evaluated against a planar Ni electrode also prepared by electrodeposition. Micrometer-scale dimpled features were selected to evaluate their impact on oxygen bubble growth and coalescence, as well as to evaluate how a dimpled morphology may influence the performance of the OER. A series of Ni electrodes each with arrays of dimpled features were created by combining the self-assembly of spherical poly(styrene) (PS) templates onto planar Ni electrodes and the electrodeposition of Ni around these spherical templates. The PS templates were selectively removed from the textured Ni surfaces by dissolution in an organic solvent. The geometric dimensions and roughness of these dimpled Ni structures were characterized before and after the electrochemical measurements by scanning electron microscopy (SEM), atomic force microscopy (AFM), and water contact angle (WCA) measurements. Elemental compositions of the dimpled Ni surfaces were analyzed by X-ray photoelectron spectroscopy (XPS) and Auger electron spectroscopy (AES). Electrochemical properties, including efficiency towards the OER, were assessed by cyclic voltammetry (CV), linear sweep voltammetry (LSV), and CA measurements.

Results and Discussion

Motivations for an Investigation of a Regular Dimpled Electrode Morphology

The formation of intentionally designed microstructures that can more effectively nucleate and evolve oxygen gas bubbles is important for electrolytic processes.[20] In general, it is recognized that gas bubbles tend to nucleate in micro and nano-cavities on electrode surfaces,[21] but less is known about whether there is an optimal geometry and dimension of these cavities. Previous work in catalytic-based micro-motors have also shown that bubbles preferentially

6

nucleate on concave features rather than on convex features.[22] It is understood that bubble

nucleation requires supersaturation of O_2 to overcome the surface tension of the electrolyte

medium.[21] Concave cavities that contain pre-existing or trapped bubbles could, therefore, serve

as the initial sites for bubble generation.[23–25] It is also possible that cavities with a confined

geometry may experience a faster increase in the local concentration of O_2 during the early

stages of electrocatalytically driven oxygen evolution, achieving supersaturation and bubble

coalescence faster than flat surfaces.[26] Concave structures may act to provide sites of increased

bubble production, but these sites could become problematic if the bubble cannot easily vacate

from the surfaces. The forces that dictate bubble detachment would have to be carefully tuned in

order to appropriately use concave geometries as bubble production sites.[21] The series of regular

dimpled features presented in this work were used to investigate how concave geometries with

varying degrees of confinement influence the electrocatalytic evolution of oxygen gas.

A series of dimpled Ni surface features were prepared and evaluated for their impact on

the efficiency of the OER. In this study, regular dimpled surface features were compared as a

function of changes in their morphology since, as discussed above, previous work has suggested

a preferential nucleation of bubbles in concave features.[22, 26] Although we are not able to discern

bubble nucleation, the dimpled features enable an investigation into how these cavities influence

the dynamics of bubble growth and detachment through electrochemical analyses. A series of

four distinct concave features, each with a different degree of confinement as determined by their

height and the nominal diameter of the opening into each dimpled feature, were produced from

the same PS template (Figure 1). For example, the dimples with the tallest features exhibited the

highest degree of confinement. These four types of dimpled features were compared to planar Ni

electrodes. The dimpled features were prepared by the electrodeposition of Ni against 1.0-µm
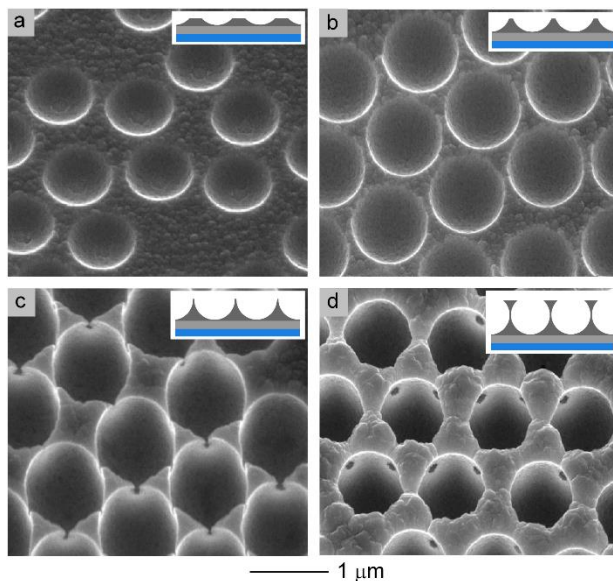
diameter spherical PS templates. The PS templates were subsequently removed, revealing dimpled Ni features on the surfaces of the electrodes. Micrometer-scale PS templates were selected to test the lower end of the microscale, specifically targeting features greater than the nanoscale and less than macroscale foams previously studied in the literature.[27, 28] The PS spheres were specifically chosen as the template due to their relatively uniform size distribution, spherical morphology, and ease of use in self-assembly processes to prepare well-ordered arrays of these templates. The PS templates provided a platform to systematically produce regular arrays of dimpled textures on the Ni electrodes with fine-tuned feature heights to change the degree of confinement. Modifications to the surface morphology with electrochemical processing and aging of the Ni electrodes were also easily discerned due to the regularity of these surface features.

Formation of Regular Dimpled Features in Ni Surfaces

The regular dimpled features were prepared by electrodeposition of Ni around a two-dimensional self-assembled array of spherical 1.0-µm diameter PS templates. The experimental methods for the formation of regular dimpled features can be found in the Supporting Information file. The protocol for the self-assembly of the PS spheres was adapted from Moon *et al.*[29, 30] Spherical PS templates can readily form close-packed monolayers at an air-water interface, which can be transferred to an electrode using a lift-out method. Assembly of PS spheres at an air-water interface was selected as the method to prepare the arrays of templates for several reasons: (i) a uniform close-packed assembly quickly forms at the air-water interface; (ii) the assembled PS template is easily transferred to a solid support by a lift-out process; (iii) the self-assembly procedure favors the formation of a monolayer; and (iv) several substrates can be

coated with the PS templates obtained from a single assembly at the air-water interface. Using this method, close-packed arrays of the PS spheres were quickly and reproducibly prepared on the Ni substrates (Figure S1 of the Supporting Information, SI). The fraction of the Ni substrates covered by the spherical templates was calculated to be $67 \pm 2\%$. Electrodeposition of Ni around these spheres was used to prepare a series of textured, regular Ni surface morphologies.

Figure 1. Representative scanning electron microscopy (SEM) images of textured nickel (Ni) electrodes prepared using spherical poly(styrene) (PS) templates. These images correspond to the (a) 1/4 structures, (b) 1/3 structures, (c) 1/2 structures, and (d) 3/4 structures prior to electrochemical testing. All samples were imaged at a 35º tilt. The inset schematics depict the heights of the Ni features relative to the 1.0-µm diameter PS templates.

Four distinct surface morphologies were prepared by electrodeposition of Ni in the regions between the spherical PS templates (Figure 1). A planar electrode prepared by electrodeposition of Ni onto the Ni electrodes without the use of a PS template was used as a control sample. The morphology of the dimpled Ni features are described by the height of the

electrodeposited Ni relative to the diameter of the PS spheres, and are thus referred to as 1/4, 1/3, 1/2, and 3/4 structures. Varying the height of these features resulted in a change in the degree of confinement within the dimple, as well as the diameter of the opening between the recesses of the dimples and the bulk electrolyte solution. The feature height was controlled by adjusting the duration of the electrodeposition process under potentiostatic conditions at -1.0 V versus a saturated calomel electrode (SCE). The evolution of the current as a function of time during electrodeposition, also referred to as a growth curve, is shown in Figure 2. Changes to the Ni morphology were correlated to the potentiostatic growth curve by stopping the electrodeposition process at particular time points and analyzing the structured electrodes through SEM measurements. The area of each electrode immersed in the plating solution during the electrodeposition process was kept constant. The magnitude of the current is proportional to the surface area in contact with the plating electrolyte and the rate of Ni electrodeposition.[31] Reproducing the shape and locations of the peak in the growth curves largely depends on the uniformity of the assembled polymer templates and variations in the resistance of the exposed surfaces, such as from variable coverage with surfactants (e.g., PVP). The observed current response in Figure 2 is representative of the general shape of other growth curves, and reflects the variable path of mass-transport that occurs during electrodeposition around the PS templates. The current decreases until reaching 130 s, upon forming the 1/3 structures due to a decrease in the electrode surface area exposed to the electrolyte between the adjacent PS spheres. Diffusion of electrolyte to the electrode is restricted for the 1/3 structures because of the decreased volume of electrolyte in proximity to the electrode, and the restricted diffusion of electrolyte through the narrow channels between the close-packed spheres. It is estimated that the current density within these narrow channels upon reaching point b in Figure 2 (at 130 s) was -4.7 mA/cm^2, which

accounts for the openings between the self-assembled spheres. The flux of electrolyte increased for the subsequent structures as the channels widened with increasing thickness of the Ni relative to the PS templates (e.g., 1/2 structures), which resulted in an increase in the current. The time points determined from the potentiostatic growth curve, as verified by SEM, were used as a guide to reproducibly prepare each of the four types of electrodes with the desired features. The final features were also verified by SEM for each of the tested electrodes.
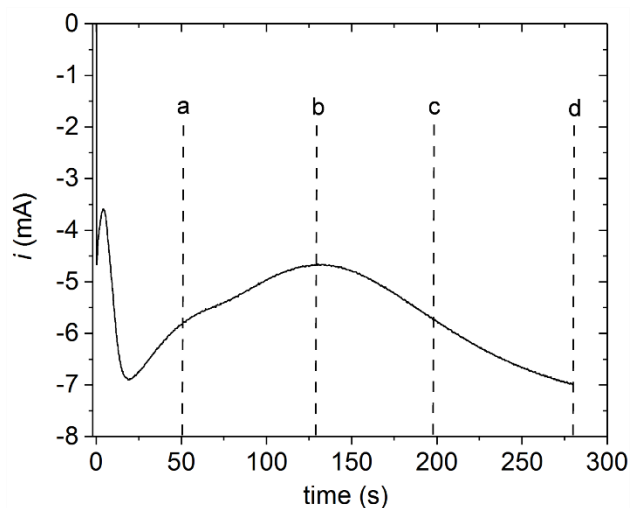
Figure 2. Representative potentiostatic growth curve for the textured Ni electrodes during electrodeposition of Ni at -1.0 V versus SCE. The dashed lines indicate the time points at which the (a) 1/4 structures (50 s), (b) 1/3 structures (130 s), (c) 1/2 structures (200 s), and (d) 3/4 structures (280 s) were prepared during the electrodeposition process.

Morphology of Regular Dimpled Features Before Electrochemical Testing

The morphology of the dimpled Ni surface features were evaluated by SEM after removal of the PS templates. Distinct morphological features are observed by SEM (Figure 1). The average height of the dimpled features was determined by measuring the average radius, a, of the dimpled features with a 0º tilt (Table 1) and applying a spherical cap model (Section S1 in

11

the SI). The mean radii of the opening into the confined features varied between 430 and 500 nm giving heights between 245 and 737 nm (Table 1). The dimples in the 1/4 and 1/3 structures were the most similar to a typical concave morphology, see Figures 1a and 1b. As expected, the flat regions between the dimpled features in the 1/4 structures had a large contribution to the electrodeposited surface area. The contribution from flat surface area between the dimples was the smallest for the 1/2 structures when compared to the other three structured electrodes (Figure S2). Electrodeposition of Ni to half the height of the templates is indicated by the interconnected channels that are partially formed at the ridges between the 1/2 structures in Figure 1c. Further electrodeposition of Ni to prepare the 3/4 structures show the well-defined interconnected pores between the dimpled structures as a result of the close-packing of the PS templates. The interconnected pores observed in the structures taller than the 1/3 structures were formed at sites where electrodeposition was inhibited by the contact between adjacent PS spheres. The 3/4 structures were the most confined concave structures evaluated in this study, with the opening into each dimple having an average diameter of 440 nm and each dimpled feature an average depth of 737 nm.

Table 1. Dimensions of dimpled features as determined by SEM and atomic force microscopy (AFM) measurements.

	planar Ni	1/4 structures	1/3 structures	1/2 structures	3/4 structures
average radius of dimpled opening (a)	N/A	430 nm	475 nm	500 nm	440 nm
average height of spherical cap (h)	N/A	245 nm	344 nm	500 nm	737 nm
R_{AFM}	1.4 ± 0.5	1.3 ± 0.0	1.5 ± 0.4	1.2 ± 0.1	1.6 ± 0.1
R_f	1.42	1.39	1.49	1.82	2.52

Electrochemical Aging of the Ni by Cyclic Voltammetry

The regular dimpled Ni electrodes were aged by cyclic voltammetry (CV) until achieving

a consistent electrochemical behavior prior to performing a series of electrochemical tests. The

electrodes were assumed to be in a steady-state condition once the current of the anodic peak

varied at most by 10 µA over ~50 consecutive scans. This method of electrochemical aging by

CV was done to ensure that the Ni phases present at the dimpled surfaces had a minimum

variability between the samples.[19] The potential applied to the electrodes while immersed in high

purity 0.1 M KOH was scanned between -0.4 and 1.2 V versus a mercury/mercury oxide

electrode (or Hg/HgO) by CV techniques (Figure 3). At -0.4 V versus Hg/HgO the surfaces

contain a Ni phase composed of β-Ni(OH)$_2$.[32, 33] The first peak in the forward scan, which was

located at 0.45 V, is attributed to the reversible oxidation of β-Ni(OH)$_2$ to β-NiOOH. The

cathodic peak at 0.28 V in the reverse scan is the reduction of β-NiOOH and formation of the β-

Ni(OH)$_2$ phase. The β-Ni(OH)$_2$/β-NiOOH layers grow in thickness with consecutive CV

scanning as water, protons, electrons, and hydroxide ions are transported to and from the bulk

electrolyte throughout this redox process.[34–36] The suggested redox process starts with the

removal of protons from the β-Ni(OH)$_2$ prior to oxidation and formation of the β-NiOOH

species.[34] These protons combine with hydroxide ions to form water at the interface between the

electrode surfaces and the electrolyte. Upon reduction, the dissociation of water molecules

produces protons that diffuse back into the structure, while hydroxide ion electrolyte is driven

out of the surfaces with the change in structure. The redox processes are kinetically limited, but

is facilitated by the applied potential and diffusion of the electrolye.[37] The growth of the β-

Ni(OH)$_2$/β-NiOOH phases on the surfaces of the electrodes, or the formation of the layered

double hydroxide (LDH) phase, is reflected by a shift in the anodic and cathodic peak potentials to higher and lower potentials, respectively, and an increase in the current density. [32, 37] Additional CV plots for the planar Ni, 1/3 structures, 1/2 structures, and 3/4 structures can be found in Figure S3. Achieving a steady-state condition for Ni-based electrodes indicates that the relative amount of reduced β-NiOOH and oxidized β-Ni(OH)$_2$ are no longer changing with each consecutive CV scan. Since the β-NiOOH is considered to be the active phase responsible for the OER activity of Ni,[38] an electrode that has been aged to form a uniform and stable β-NiOOH phase was desired to assess the electrochemical efficiency of each type of dimpled electrode.
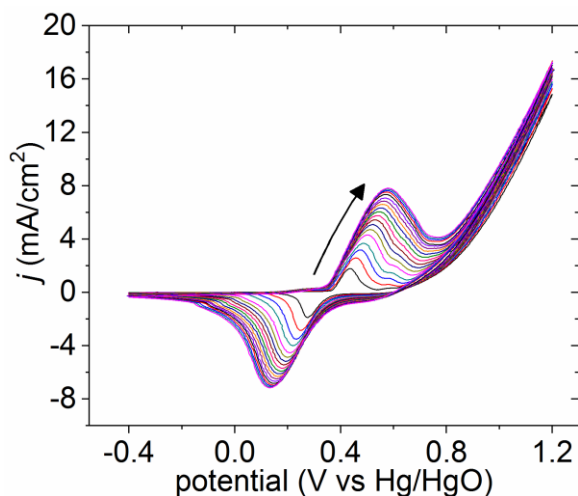
Figure 3. Electrochemical aging of the 1/4 structures by cyclic voltammetry (CV). The data was acquired in high purity 0.1 M KOH at a scan rate of 50 mV/s. Every 100th CV profile is shown.

Diffusion effects can play a role in the characteristics of the CV scans, especially if convective mass transfer of electrolyte is not imposed by another means, such as the stirring of electrolyte.[39] Diffusion limited effects of the electrolyte are more pronounced at high CV scan rates, which can cause a distortion in the features observed in the CV plots.[40] Anodic and cathodic peaks observed in the CV plots can be more prone to distortion when several proton-

coupled electron transfer steps are needed to complete a reaction, such as in the OER.[41] The use of fast CV scan rates typically require the use of a microelectrode to minimize changes in the resistivity of the system due to contributions that otherwise result from localized transport limitations, and specialized potentiostats are used to minimize peak distortion.[42] These specialized potentiostats are typically equipped with large bandwidth capabilities, high-speed amplifiers, and the capacitance from the system is reduced by elimination of excess switches. In this work, relatively slow scan rates (50 mV/s, Figure S3) were used to acquire a series of CV scans to better visualize the evolution of the anodic and cathodic peaks. The electrochemical aging process used a higher scan rate of 100 mV/s. After every set of 100 scans recorded at 100 mV/s, 10 scans were recorded at the slower scan rate of 50 mV/s. The CV plots obtained at 50 mV/s enabled a comparison of the effects of the electrode surface morphologies on the near surface diffusion of the electrolyte. For example, the CV profiles for the planar Ni electrode exhibit sharper anodic and cathodic peaks than those for the electrodes with the 3/4 structures. Hindered diffusion is likely a major cause of the progressive broadening observed for the peaks in the CV scans from the 1/4 to the 3/4 structures.

Shifts in the anodic and cathodic CV peak potentials are typical during electrochemical aging of $Ni(OH)_2$ surfaces in alkaline media.[43] Upon cycling of the planar Ni and 1/4, 1/3, and 1/2 structured electrodes, the anodic and cathodic peaks grow in their intensity and shift to higher potentials (from 0.45 to 0.60 V) and lower potentials (0.28 to 0.15 V), respectively. The 3/4 structures had the greatest shift between the first and last CV scan for the position of the anodic (0.49 to 0.90 V) and cathodic (0.22 to -0.11 V) peaks. The broadening of the peaks for the 3/4 structures is likely due to a slower rate of electrolyte diffusion to all of the electrode surfaces because this structure has the greatest ECSA and the deepest dimpled features. Because the

15

conversion from β-Ni(OH)$_2$ to β-NiOOH is limited by electrolyte diffusion to all of the surfaces of the electrodes, the resistance effectively increases with progressive formation and growth of the LDH phase. An increase in the resistance across the interface of the electrodes shifts the oxidation and reduction peaks in the CV profiles as the passivating β-Ni(OH)$_2$/β-NiOOH phases increase in thickness over the surfaces of the electrode.[37] The larger shift in peak potentials observed in the CV scans for the 3/4 structures is attributed in part to the relatively high scan rates. The 3/4 structures are more susceptible to deviation from the anticipated CV peak character with formation and growth of the LDH phase since the majority of the ECSA is confined within the recessed dimples. It is also possible that an uneven wetting of the surfaces within the 3/4 dimpled features could cause broadening of the peaks due to local variations of pH at the surfaces.[44] Furthermore, growth of the LDH phase with prolonged electrochemical aging induced a change in the surface morphology of the electrodes.

Surface Morphology After Electrochemical Aging

The surface morphology of the Ni electrodes changed after electrochemical aging with formation of the LDH phase of β-Ni(OH)$_2$/β-NiOOH. After electrochemical aging, the arrays of dimpled features transformed into highly textured surfaces with a "flakey" appearance (Figure 4 and Figure S4). The features within these new textures correlated well with the dimpled structures. The 1/4 and 1/3 structures were covered with relatively small flakes (142 ± 41 nm and 134 ± 34 nm wide ridges, respectively), while the 1/2 structures were coated with the largest flakes around 315 ± 94 nm wide and the 3/4 structures were coated with medium flakes having a width of 222 ± 52 nm. The surface morphology of the planar Ni also exhibited a textured surface morphology with electrochemical aging (Figure S5). The structural transformation to the LDH

phase and the corresponding increase in roughness and texture may also provide better accessibility of electrolyte to active sites on the electrode surfaces.[45] The LDH β-Ni(OH)$_2$/β-NiOOH phase often resembles a roughened nanoscale texture on both planar electrodes and Ni hydroxide nanoparticles when examined by electron microscopy.[46–48] The textures observed in these previous studies are similar to those found on the dimpled Ni electrodes after electrochemical aging. Hydrous oxides are typically amorphous and can take on many different morphologies. Several factors can impact the morphology of these hydrous oxides, such as electrolyte concentration, pH, temperature, and in some cases the presence of other metal species or solvent molecules within the LDH phase. [6, 49]
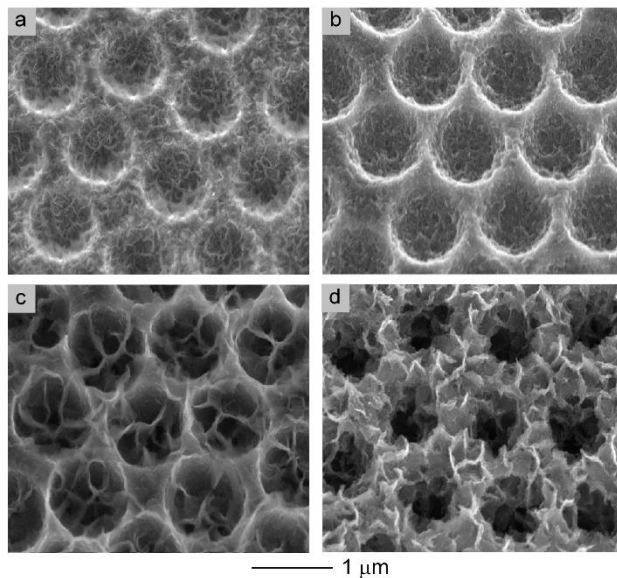
Figure 4. Representative SEM images of the textured Ni electrodes after electrochemical aging as depicted for the (a) 1/4 structures, (b) 1/3 structures, (c) 1/2 structures, and (d) 3/4 structures. All samples were imaged at a 35° tilt.

Composition Before and After Electrochemical Cycling

The OER activity of transition metals can be influenced by many factors including their composition. The composition of the electrodes was analyzed by XPS both before and after electrochemical cycling (Figure S6). This analysis enabled an evaluation of the presence of trace elements at the surfaces of the electrodes. All chemical components found in the XPS survey scans are summarized in Table S1. The electrochemically aged Ni electrode shows an increase in the intensity of the O 1s species relative to the as-prepared planar Ni due to the presence of β-Ni(OH)$_2$ and β-NiOOH on the electrode surfaces after electrochemical cycling. After electrochemical aging, the Ni peaks and the Ni Auger transitions are also more pronounced in the XPS analysis. This increase is likely due to the higher Ni surface area of the flakes on the aged electrodes, as well as the removal of trace amounts of organic surfactants that remained from the templating process. The removal of trace organics after electrochemical aging is also demonstrated by a decrease in the intensity of the C 1s peak after the aging process. These surfactants are removed during electrochemical processing in the alkaline conditions of the electrolyte. Strong Ni LMM transitions occur at binding energies (BE) of 773, 709, and 638 eV, and overlap with the Co 2p, Fe 2p, and Mn 2p signals, respectively. Analysis and assignment of the chemical state for the first-row transition metals by XPS can be challenging due to the metal 2p spectra. Plasmon loss structure, multiplet splitting, and shake-up structure can lead to complex curve-fittings required for interpretation of these spectra.[50] The XPS analysis was unable to adequately discern the presence or absence of these transition metals, which could dramatically influence the wetting and catalytic activity of the electrodes.[8, 51, 52] Auger electron spectroscopy (AES) was, therefore, used as a complementary technique to further investigate the

possible presence of transition metal impurities that may alter the electrochemical properties of the Ni electrodes.

First-row transition metals have a higher probability of Auger electron emission in comparison to X-ray induced photoelectron emission.[53] Auger electron spectroscopy was, therefore, used for analyzing the surface composition of the electrochemically aged electrodes. The AES scan identified three prominent Ni LMM transitions at kinetic energies (KE) of 849, 777, and 719 eV (Figure S7). Although a single Fe LMM transition overlaps with the Ni LMM transition at 719 eV, the two other prominent Fe LMM transitions are typically observed at 594 and 654 eV are not present in the spectrum.[54, 55] The lack of distinct Fe Auger transitions that do not overlap with the Ni LMM peaks suggests that Fe impurities are either not present in the surfaces of the Ni after the aging process, or are below the detection limits of this surface spectroscopy technique. The results were similar for the $L_3M_{2,3}M_{2,3}$, $L_3M_{2,3}M_{4,5}$, and $L_3M_{4,5}M_{4,5}$ Co transitions, which occur at 656, 716, and 775 eV, respectively.[56] Two of the Co transitions overlap with Ni $L_3M_{2,3}M_{2,3}$ and $L_3M_{2,3}M_{4,5}$ transitions at 719 and 777 eV, but the characteristic Co transition at 656 eV is absent from the AES survey scan. A summary of the Auger transitions and their respective energies can be found in Table S2. The absence of distinct Fe and Co peaks is a strong indication that these impurities in the aged Ni electrodes are not detectable by AES. It can, therefore, be concluded that the differences in the electrochemical properties observed between the different types of structured electrodes were not due to variations in their compositions (e.g., Fe content), but instead due to changes in their surface morphology.

Determination of the Theoretical Surface Area for Regular Dimpled Ni Features

The theoretical ECSA was calculated for the regular dimpled surface features from a morphological analysis. Parameters for this determination were obtained from the electrodes before electrochemical aging using a combination of SEM and atomic force microscopy (AFM) measurements. The roughness factor for the flat regions between the dimpled features (R_{AFM}) was quantified by AFM for each of the structured electrodes before electrochemical aging (Table 1). The mean R_{AFM} for each electrode was calculated by averaging five separate R_{AFM} measurements each over an area of ~0.92 μm^2. The R_{AFM} was greatest for the 3/4 structures (i.e. 1.6), while the lowest value was calculated for the 1/2 structures (i.e. 1.3). The surfaces inside of the dimpled features appeared to be smooth when assessed by SEM in accordance with the smooth spherical PS templates used to prepare these features. In addition, the roughness measurements inside of the dimpled features could not be obtained due to the geometric limitations of analyzing these regions using the AFM probe (Figures S8 and S9). Since the dimpled features resemble the geometry of spherical-shaped cavities, a spherical cap model was used to estimate the surface areas within the dimpled features (SI, Section S1). The openings into these spherical cavities were measured by SEM, and these values were used to calculate the depth and surface area of these features. Large area SEM images for each type of electrode were used to quantify and compare the average number of dimpled features. These images were obtained over pre-defined areas of ~190 μm^2. The combination of the surface area within the dimpled features, average number of dimpled features per unit area, total area not occupied by the dimpled features, and the average R_{AFM} for the flat regions between the dimples were used to calculate the electrochemical roughness factors (R_f) for each electrode. The R_f were calculated by dividing the real surface area by the geometric surface area. The R_f values were 1.45, 1.40, 1.48,

1.83, 2.52 for the planar Ni, and the 1/4, 1/3, 1/2, and 3/4 structures, respectively. The R_f values

obtained from these measurements were used to estimate the theoretical ECSAs for each of the

structured electrodes, as well as the planar Ni electrode. These ECSA values were subsequently

used to derive the current densities that are reported for the electrochemical data. The calculated

ECSA is likely to be an underestimation of the actual value due to the impossibility of measuring

the roughness inside the dimpled features. Evaluation of the theoretical ECSA would have been

impossible if the electrodes had not been fabricated with regular dimpled features. The increased

roughness and texture after electrochemical aging presents a challenge for using the same

approach to estimate the ECSA. It is expected that the trends observed for the ECSA for the as-

prepared samples are maintained, but that the absolute values will be greater after

electrochemical aging due to the increased roughness.

Wetting Behavior of Regular Dimpled Ni Electrodes by Contact Angle Measurements

The wettability of the dimpled Ni electrodes was characterized by equilibrium contact angle

(θ) measurements obtained both before and after electrochemical aging. The dynamics of gas

bubble release from the electrode surfaces can be adjusted by tuning its wettability.[4] It has been

previously demonstrated that microstructures with features on the order of 20 µm and surfaces

with hierarchical structures (e.g., nano- and microscale) may sufficiently modify the wetting

properties and, indirectly, bubble release properties from Ni electrodes.[10, 19] Surfaces exhibiting a

low surface tension (hydrophilic, $\theta < 90°$) at the interface between the solid electrode and

electrolyte solution can improve the OER current density in comparison to more hydrophobic

surfaces.[5, 12] The as-prepared, dimpled surfaces were each similarly hydrophobic with water

contact angles (WCAs) around 96°, while the planar Ni had a WCA of 87° (Figure S10). The

regular dimpled texture increased the hydrophobicity of the Ni surfaces before electrochemical aging. After the electrochemical aging processes, the electrodes demonstrated a high degree of wettability (Table S3), becoming more hydrophilic. Hydrophilic surfaces with WCA close to 20° were measured for all of the dimpled and planar electrodes after electrochemical aging. The presence of the β-Ni(OH)$_2$/β-NiOOH phases covering their surfaces, as well as the increase in their nanoscale roughness, likely facilitated the increased wettability of the Ni surfaces.[57–59]

Contact angle measurements obtained using the electrolyte, 0.1 M high purity KOH, were similar to the WCA values, but exhibited even lower values for all of the samples both before and after electrochemical aging (Figure S11). Stronger attractive forces between the surfaces of the electrodes and the electrolyte are responsible for the increased wettability when the solution of KOH is used for the contact angle measurements. The oxides and oxy-hydroxides on the electrode surfaces interact more favorably with the ionic basic electrolyte (pH 13) than with the slightly acidic (pH 6) deionized water used in the CA measurements. The electrode surfaces are hydrophilic after electrochemical aging, indicating that the supply of electrolyte to all surfaces of the electrodes was potentially sufficient during the OER.

Theoretical wetting models were compared to the experimental water contact angles for the electrodes obtained prior to the electrochemical measurements. A highly wetting state for a solution can be described by a Wenzel model.[13] This model can describe the complete contact between rough surfaces and a sessile droplet of liquid during the contact angle measurement. In contrast to the Wenzel state, air might be trapped underneath the liquid droplet where only the topmost features of structured surfaces are wetted with the solution. This scenario is often described as a Cassie-Baxter state.[60] The Cassie-Baxter model can be used to describe a roughened surface with chemical heterogeneity, while the Wenzel model can describe a rough

surface that is chemically homogeneous.[61] An analysis using experimentally derived roughness factors indicates that these models are insufficient to describe the wetting behavior observed for the textured Ni surfaces (SI, Section S2). The planar Ni electrode prior to electrochemical aging had a wettability close to that predicted by the Wenzel model, but the structured Ni surfaces deviated from the trend predicted by the Wenzel model. This deviation indicated a partial wetting of the electrode surfaces. When comparing the contact angle data obtained before the aging process to the trend predicted by the Cassie-Baxter model, the planar Ni electrodes and the 1/4 structure were the closest fit to this model. For the other structures, the model predicted contact angle values that were higher than the experimental values, again indicating partial wetting of the electrode surfaces. This deviation from both the Wenzel and Cassie-Baxter models indicates that the structured electrodes are in a mixed state (e.g., a non-ideal Cassie-Baxter state) in which air bubbles are partially filling some of the dimples. The planar electrode exhibited properties that were the closest to a fully wetted state, but some air bubbles might also be trapped in the recesses of these relative rough surfaces of electrodeposited Ni.

A comparison of the water contact angle measurements obtained after electrochemical aging of the samples to the values predicted by the models is complex due to the enhanced surface roughness of the surfaces with growth of the LDH phase. Differences in the wettability of each of the electrodes after electrochemical aging were difficult to discern due to variations in the roughened surface textures. It was not possible to perform a reproducible characterization of the resulting surface morphologies, which were needed to obtain geometrical parameters for each of the models. A comparison of the experimental results for the aged electrodes to the values predicted by the Wenzel and Cassie-Baxter models was, therefore, not feasible. Films of β-NiOOH with similar structures to the surfaces of the aged Ni electrodes showed similar

hydrophilic contact angles. [57, 59, 62] Based on the known hydrophilicity of the β-Ni(OH)$_2$/β-NiOOH phases, it is expected that a smaller amount of air would be trapped in the dimples or on the surfaces of the aged electrodes than on the as-prepared electrodes.

Assessing the Efficiency of the Oxygen Evolution Reaction for Regular Dimpled Ni Electrodes

The efficiency of the OER was investigated by linear sweep voltammetry (LSV) for the planar Ni and the dimpled Ni electrodes. The theoretical ECSA values determined before electrochemical aging were used for normalization of the current in units of current density (mA/cm^2). This normalization enabled a more exact correlation of the differences in the surface morphology to their electrochemical performance for the OER. Normalizing the observed current against the theoretical ECSA, instead of using the geometrical area of the electrode, considers the additional catalytic surface area from the dimpled textures and provides a more accurate comparison of the observed activities toward the OER. Five separate LSV measurements were recorded for each electrode and the mean current densities for each type of electrode are plotted in Figure 5. Directly following each LSV measurement, five CV scans were recorded to reestablish a stable electrochemical state. A scan rate of 1 mV/s was chosen for the LSV profiles to allow for adjustments to the mass transport in the electrolyte with changes in the applied potentials, and to minimize shifts in the peak potential.[60] The current begins to rise as the voltage is scanned past 0.7 V versus Hg/HgO for all of the electrodes. As the potential increases beyond 0.7 V versus Hg/HgO, differences in OER performance between each of the dimpled structures become more evident. The mass transport effects also become more significant at higher potentials. The influence of surface morphology on bubble formation and release will, therefore, be reflected in the current density generated at these higher applied potentials.

The performance of the dimpled Ni electrodes were further evaluated by comparing their Tafel plots. This assessment used the Tafel equation, $\eta = b \times \log(j/j_0)$, where η is the overpotential, b is the Tafel slope, j is the current density, and j_0 is the exchange current density.[63] Anodic Tafel curves were derived from the data obtained from the LSV experiments (Figure S12). The oxidation of Ni (II) to Ni (III) and Ni (IV) observed at ~0.53 V vs Hg/HgO was omitted from the Tafel curves. Linear fits were applied to the regions of both low and high overpotentials for each type of electrode (Figure S13). The overpotential in the Tafel curves was determined by subtracting the OER onset potentials (Table S4), which were determined from the LSV measurements acquired at scan rates of 1 mV/s (Figure 5). A low Tafel slope and a high exchange current density are indicative of materials with a high electrocatalytic activity.[63] A high exchange current is desired to minimize the activation overpotential for the reaction. The Tafel parameters, b and j_0, were determined for both the high and low overpotential regions (Table S5). The planar and 1/4 structures had the lowest slopes with similar values for the low overpotential regions indicating that they likely had similar electron and mass transfer behavior. For the 1/3, 1/2, and 3/4 structures, the Tafel slopes increase dramatically with an increase in the depth of the concave recesses, which may signify an increase in the passivation of the Ni surfaces due to an increased residence of oxygen bubbles in the recessed regions and blocking of active surfaces. The 1/4 structures exhibited the highest exchange current densities in the high overpotential region where the rate of oxygen evolution is the highest.
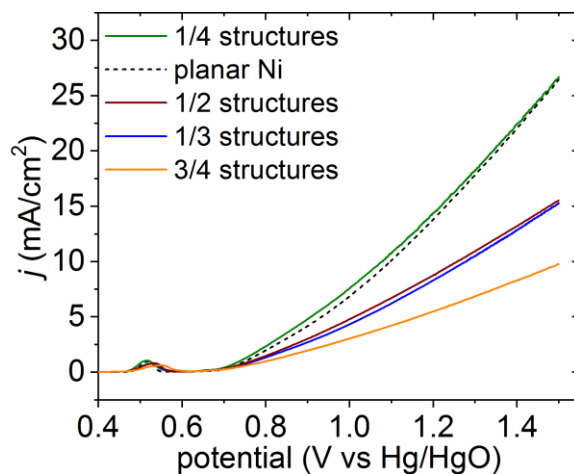
Figure 5. Assessment of the oxygen evolution reaction (OER) activity in 0.1 M KOH by linear sweep voltammetry (LSV) for a series of textured Ni surfaces prepared from 1.0-µm diameter PS templates. The LSV response of planar Ni is included for comparison. The current is normalized for each sample to its theoretical electrochemically active surface area (ECSA). All transients are plotted as an average of five independent experiments, and the current was recorded at a scan rate of 1 mV/s.

The dimpled features permit an examination of how the confinement within a 1.0-µm diameter cavity may influence the overall efficiency of the OER. Because the electrodes had identical compositions and were aged by a series of identical methods to achieve an assumed steady-state, the differences in performance observed at the higher applied potentials are anticipated to reflect the effects of changes to their surface morphology on the oxygen bubble behavior and mass transport. In a prior study on structure-function correlations of the OER, cylindrical recesses (~1-µm depth and 20-µm diameter) were found to have a higher activity towards the OER when compared to planar nickel electrodes.[19] The cylindrical recesses were also capable of reducing bubble adhesion under a lateral shear flow as predicted by Weber number calculations. In the case of a motionless electrolyte, confined geometries are likely to be

more significantly impacted by changes in fluid dynamics from bubble-induced microconvection.[64] For example, as a bubble grows, the electrolyte is pushed outwards in a radial direction and once a bubble detachment event occurs, the electrolyte will move in to fill the volume previously occupied by the departed bubble.[65] The morphology of the electrode will, therefore, play a key role in the overall efficiency of the reaction. Oxygen bubbles may adhere to or be confined within the more deeply recessed dimpled features (e.g., 3/4 structures) leading to a decrease in the overall current density at higher potentials. Bubble nucleation within more confined surface features (e.g., within the recesses of the 3/4 and 1/2 structures) could also occur at a faster rate due to the possibility of pre-existing gas in the cavities, higher levels of supersaturation, and greater proximity to ECSA.[64, 66] These bubbles could become pinned within the recesses due to this confinement and insufficient fluid dynamics to release the bubbles.

The lowest current densities for the OER were observed for the 3/4 structures in comparison to the other types of electrodes including the planar Ni electrode (Figure 5). The reduced efficiencies of the 3/4 structures may be due to the entrapment of oxygen bubbles within these recessed features. Limited diffusion of electrolyte into the 3/4 structures may also play a role in their decreased performance for the OER. The 1/4 structures demonstrated the highest efficiency for the OER when compared to the 1/3, 1/2, and 3/4 structures. The planar Ni electrode had a similar performance to the 1/4 structures, which may be due to the similar surface morphologies of these two types of electrodes after electrochemical aging. Prior to the electrochemical measurements, the planar Ni and 1/4 structures demonstrated the highest degree of wetting with both water and electrolyte. The wettability of the planar and 1/4 structures, relative to the other dimpled structures, may be linked to their improved efficiency for the OER. Stabilization of oxygen bubbles could be more challenging on the surfaces of the electrodes that

27

have a more planar geometry. The arrays of dimples with deeper recesses may more easily trap

bubbles within their cavities, which could hinder mass transport and prevent bubbles from

efficiently being released from their surfaces.

Dimpled electrodes with the 1/3 and 1/2 structures closely follow the same trends as the

1/4 structures and exhibit higher current densities than the 3/4 structures. The difference in

height of the features within the 1/3 and 1/2 structures did not result in any measurable

differences in the OER efficiency as observed by the LSV experiments. The mass transport of

electrolyte and the oxygen bubble release kinetics from the electrode surfaces are likely to be

similar for these two types of dimpled structures based on the potential sweeps during the OER

as examined by the LSV measurements. Although the LSV experiments are useful for assessing

the performance of electrodes for the OER over a wide range of applied potentials, additional

experiments are necessary to probe their properties under prolonged operation.

Chronoamperometry (CA) experiments were used to investigate the performance of the various

types of electrodes over longer periods of time while operating at high potentials for the OER.

Chronoamperometry of Regular Dimpled Ni Surfaces

Steady-state performance of the Ni electrodes towards the OER was probed by constant

potential CA experiments. An applied potential held constant for a sufficient duration of time can

allow for stabilization of the reaction kinetics, adsorption processes, and mass transport. The

electrodes were held at a potential of 1.2 V (vs. Hg/HgO) for 1 h to enable equilibration of these

processes during the OER and to assess their long-term efficiencies (Figure S14). A potential of

1.2 V was chosen because it is the midpoint between the low and high ends of the OER region in

the LSV profiles. Mass transport occurred by diffusion to and from the dimpled structures with

the electrode held in a vertical orientation within a stagnant electrolyte. The CA profiles in Figure 6 were each considered to reach a steady-state condition as the current densities stabilized over time. More pronounced differences were observed in the steady-state CA profiles than for the LSV experiments. These differences were attributed to the equilibration of mass transport processes related to both the electrolyte diffusion and gas evolution. The relative performance of each type of electrode largely followed the same trend observed in the LSV experiments. The CA experiments further confirmed that the OER performance of the 1/4 structures is superior to the planar Ni electrodes. The 1/4 structures demonstrated the highest overall current density and the highest amplitude of the oscillations in their current density. More frequent oscillations in the amplitude of the current density have been linked to a faster bubble release, while the amplitude of these oscillations are proportional to the size of the bubble or to the amount of bubbles simultaneously released from the surfaces of the electrode.[19, 67] The planar Ni had a similar performance to the 1/4 structures. Although the planar and 1/4 structures have the most similar morphologies, the better performance of the 1/4 structures may be attributed to its array of ~245-nm deep concave recesses. The processes of bubble formation and release may be stabilized by the curvature, regularity, and spacing of the concave recesses of the 1/4 structures resulting in its larger current and the periodic changes in its amplitude as observed in the CA measurements. In fact, the planar electrodeposited regions between the recesses may improve the effects of convective mass transfer, since both the electrolyte and dissolved gas can move freely across the planar surfaces to the dimpled sites.[65, 68] The dimples in the 1/4 structures were more exposed to the lateral or free motion of electrolyte and dissolved gas than for the other dimpled electrodes, which could cause a larger number of bubbles or a larger diameter bubble to be released in accordance with the observed oscillations in current amplitude. Based on these results and the

previous literature,[21, 25, 69] it is hypothesized that there may be an ideal length of time for a bubble to reside on the surfaces of the electrodes for balancing the processes associated with transport of the dissolved gas species for bubble nucleation and growth with the processes for release of bubbles from these surfaces. The curvature, diameter, depth, and spacing of the dimpled features are each likely to facilitate the processes related to the observed improvement in the OER for the 1/4 structures.
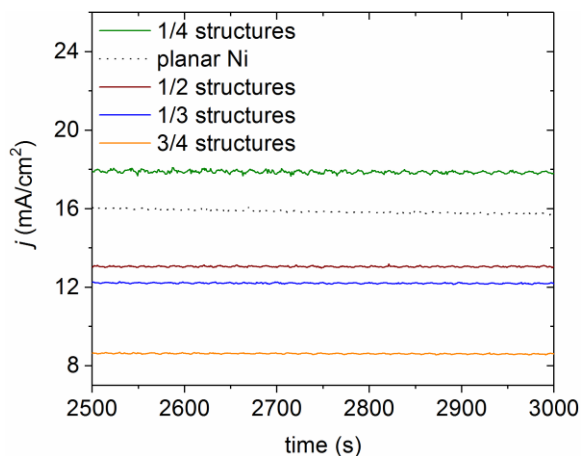
Figure 6. Chronoamperometry of the textured and planar Ni electrodes measured at 1.2 V versus Hg/HgO over a period of 500 s.

Dimples with deeper recesses may stabilize the oxygen bubbles for longer durations than are ideal causing a drop in the overall current density. Subtle modifications to the depth of the dimpled features can hinder gas evolution from their surfaces. The oscillations in the amplitude of the CA measurements for the 1/3, 1/2, and 3/4 structures are less distinct, but seem to occur at a similar frequency. The 1/3 and 1/2 structures, which are more confined than the 1/4 structures, show a reduced performance towards the OER. The decrease in overall performance for the 1/3 and 1/2 structures indicates that a dimple depth of ~344 nm is sufficient to pin bubbles to the electrodes and effectively reduce the ECSA. The observed difference in current density (e.g., ~1

mA/cm^2) between these two structures could be negligible. The slightly higher current density in the CA profiles of the 1/2 structures may also suggest that the change in the morphology could contribute to an improvement in bubble release. The features in the 1/2 structures are in closer proximity, which may enable the bubbles to more easily coalesce and subsequently release from the electrode surfaces. The 3/4 structures exhibited the poorest efficiency for the OER as observed in their CA profiles. These electrodes had the most confined geometry within their concave recesses, such that fresh electrolyte had limited access to all of the surfaces within these dimples. Excessive pinning of bubbles to the surfaces within the recesses of the 3/4 structures may also impede release of gas bubbles.

The results from this study suggest that dimpled or recessed features on the order of 1.0 µm in diameter and with depths of at least ~344 nm have a higher propensity to trap bubbles causing high overpotentials and inefficiencies associated with mass transport processes during the OER. Concave surface features with depths greater than ~245 nm exhibited a greater adhesion to the evolved bubbles in the absence of a shear flow as inferred from the electrochemical measurements. It is concluded that a partial wetting state, where air bubbles partially fill some of the recessed surface features, is likely to occur for each of the electrodes evaluated in this study. The WCA measurements for the planar Ni and 1/4 structures were only slightly lower than for the other types of dimpled electrodes. The improved performance of the 1/4 structures also indicates that relatively shallow dimples surrounded by planar regions of electrodeposited Ni could enhance the OER by balancing the processes of bubble growth and mass transfer induced by the lateral flow of electrolyte with bubble release. Differences in electrochemical performance observed within this series of tuned morphologies indicates that subtle variations in surface structure of the Ni electrodes can affect performance of the OER.

Surface morphology should be considered when designing electrodes with an improved

efficiency for the OER. Additional investigations will, however, be necessary to further evaluate

the utilization of both nano- and microscale features and to create a more complete

understanding of how the structure of Ni electrodes influences their electrochemical properties.

Conclusion

Uniformly dimpled textures on the surfaces of Ni electrodes prepared with well-defined

feature heights enabled a direct correlation between the structure and performance of these

electrodes for the OER. Both composition and electrochemical aging of a series of structured and

planar Ni electrodes were carefully controlled to evaluate the effects of the changes in electrode

morphologies on their efficiency for the OER. The regular concave morphologies of the dimpled

textures enabled a determination of the theoretical surface areas using measurements obtained

from a combination of AFM and SEM data. These surface areas were used to more accurately

calculate current densities, which was necessary to assess the structure-function relationships of

these electrodes. The 1/4 dimpled structures and planar Ni electrodes both outperformed the 1/3,

1/2, and 3/4 dimpled features during the LSV measurements. The deeper recesses of the 1/3, 1/2,

and 3/4 structures likely caused a decrease in their OER efficiencies due to trapped oxygen

bubbles blocking active sites within the dimples, and reduced flow of electrolyte within these

dimpled features. The 1/4 dimpled structure had the highest efficiencies for the OER under

steady-state conditions as measured by CA over an extended period of time. Larger oscillations

in the amplitude of the current were also observed for the 1/4 structures during the CA

measurements. These oscillations likely indicate the release of larger oxygen bubbles or a more

frequent release of oxygen bubbles from the surfaces of this type of electrode. Further studies are warranted to investigate regular morphologies with larger features that are more equivalent to the theoretical break-off diameter of the bubbles.[70] The findings in this study encourage further investigations into additional electrode textures, as well as further development of techniques to correlate electrochemical performance with fluid dynamics at the electrode interface.

Supporting Information

The Supporting Information includes the experimental details, additional SEM images, CV profiles, results from CA measurements, Tafel plots, AFM images and associated height profiles, data from XPS and AES measurements and their analyses, and the results from the WCA and 0.1 M KOH contact angle measurements. Further details include an evaluation of the Wenzel and Cassie-Baxter wetting models, and supporting calculations for the determination of the theoretical ECSA based on SEM and AFM measurements.

References

(1)   Xu, M.; Ivey, D. G.; Xie, Z.; Qu, W. Rechargeable Zn-Air Batteries: Progress in Electrolyte Development and Cell Configuration Advancement. *J. Power Sources* **2015**, *283*, 358–371.

(2)   Rashid, M. M.; Mesfer, M. K. Al; Naseem, H.; Danish, M. Hydrogen Production by Water Electrolysis: A Review of Alkaline Water Electrolysis, PEM Water Electrolysis and High Temperature Water Electrolysis. *Int. J. Eng. Adv. Technol.* **2015**, *4* (3), 2249–8958.

(3)   Carrasco, J. M.; Franquelo, L. G.; Bialasiewicz, J. T.; Galván, E., PortilloGuisado, R. C.; Prats, M. M.; León, J. I.; Moreno-Alfonso, N. Power-Electronic Systems for the Grid Intergration of Renewable Energy Sources: A Survey *IEEE Trans. Ind. Electron.* **2006**, *53* (4), 1002–1016.

(4)   Wang, M.; Wang, Z.; Gong, X.; Guo, Z. The Intensification Technologies to Water Electrolysis for Hydrogen Production – A Review. *Renew. Sustain. Energy Rev.* **2014**, *29*, 573–588.

(5)   Zeng, K.; Zhang, D. Recent Progress in Alkaline Water Electrolysis for Hydrogen Production and Applications. *Prog. Energy Combust. Sci.* **2010**, *36* (3), 307–326.

(6)   Trotochaud, L.; Ranney, J. K.; Williams, K. N.; Boettcher, S. W. Solution-Cast Metal Oxide Thin Film Electrocatalysts for Oxygen Evolution. *J. Am. Chem. Soc.* **2012**, *134* (41), 17253–17261.

(7)   Cook, T. R.; Dogutan, D. K.; Reece, S. Y.; Surendranath, Y.; Teets, T. S.; Nocera, D. G. Solar Energy Supply and Storage for the Legacy and Non Legacy Worlds. *Chem. Rev.* **2010**, *110* (11), 6474–6502.

(8)   Louie, M. W.; Bell, A. T. An Investigation of Thin-Film Ni-Fe Oxide Catalysts for the Electrochemical Evolution of Oxygen. *J. Am. Chem. Soc.* **2013**, *135* (33), 12329–12337.

(9)   Pérez-Alonso, F. J.; Adán, C.; Rojas, S.; Peña, M. A.; Fierro, J. L. G. Ni/Fe Electrodes Prepared by Electrodeposition Method over Different Substrates for Oxygen Evolution Reaction in Alkaline Medium. *Int. J. Hydrogen Energy* **2014**, *39* (10), 5204–5212.

(10)   Lu, X.; Zhao, C. Electrodeposition of Hierarchically Structured Three-Dimensional Nickel-Iron Electrodes for Efficient Oxygen Evolution at High Current Densities. *Nat. Commun.* **2015**, *6*, 1–7.

(11)   Baum, T.; Satherley, J.; Schiffrin, D. Contact Angle, Gas Bubble Detachment, and Surface Roughness in the Anisotropic Dissolution of Si(100) in Aqueous KOH. *Langmuir* **1998**, *14* (10), 2925–2928.

(12)   Ahn, S. H.; Choi, I.; Park, H. Y.; Hwang, S. J.; Yoo, S. J.; Cho, E.; Kim, H. J.; Henkensmeier, D.; Nam, S. W.; Kim, S. K.; Jang, J. H. Effect of Morphology of Electrodeposited Ni Catalysts on the Behavior of Bubbles Generated during the Oxygen Evolution Reaction in Alkaline Water Electrolysis. *Chem. Commun.* **2013**, *49* (81), 9323–9325.

(13)   Wenzel, R. N. Resistance of Solid Surfaces to Wetting by Water. *Ind. Eng. Chem.* **1936**, *28* (8), 988–994.

(14)   Hitchcock, S. J.; Carroll, N. T.; Nicholas, M. G. Some Effects of Substrate Roughness on Wettability. *J. Mater. Sci.* **1981**, *16* (3), 714–732.

(15)   Zeng, K.; Zhang, D. Evaluating the Effect of Surface Modifications on Ni Based Electrodes for Alkaline Water Electrolysis. *Fuel* **2014**, *116*, 692–698.

(16)   Bocca, C.; Barbucci, A.; Cerisola, G. The Influence of Surface Finishing on the Electrocatalytic Properties of Nickel for the Oxygen Evolution Reaction (OER) in Alkaline Solution. *Int. J.*

Hydrogen Energy **1998**, *23* (4), 247–252.

(17)   Dávila, M.; Elizalde, M. P.; González, M.; Pérez, M. A.; Silva, R. Morphological and Electrochemical Characterization of Ni-Polyvinylchloride Composites. *Electrochim. Acta* **1998**, *44* (8), 1307–1316.

(18)   Zeradjanin, A. R.; Topalov, A. A.; Van Overmeere, Q.; Cherevko, S.; Chen, X.; Ventosa, E.; Schuhmann, W.; Mayrhofer, K. J. J. Rational Design of the Electrode Morphology for Oxygen Evolution – Enhancing the Performance for Catalytic Water Oxidation. *RSC Adv.* **2014**, *4* (19), 9579–9587.

(19)   Paul, M. T. Y.; Yee, B. B.; Bruce, D. R.; Gates, B. D. Hexagonal Arrays of Cylindrical Nickel Microstructures for Improved Oxygen Evolution Reaction. *ACS Appl. Mater. Interfaces* **2017**, *9* (8), 7036–7043.

(20)   Volanschi, A.; Oudejans, D.; Olthuis, W.; Bergveld, P. Gas Phase Nucleation Core Electrodes for the Electrolytical Method of Measuring the Dynamic Surface Tension in Aqueous Solutions. *Sensors Actuators B Chem.* **1996**, *35* (1–3), 73–79.

(21)   Jones, S. Bubble Nucleation from Gas Cavities – a Review. *Adv. Colloid Interface Sci.* **1999**, *80* (1), 27–50.

(22)   Mou, F.; Pan, D.; Chen, C.; Gao, Y.; Xu, L.; Guan, J. Magnetically Modulated Pot-Like $MnFe_2O_4$ Micromotors: Nanoparticle Assembly Fabrication and Their Capability for Direct Oil Removal. *Adv. Funct. Mater.* **2015**, *25* (39), 6173–6181.

(23)   Dean, R. B. The Formation of Bubbles The Formation of Bubbles. *J. Appl. Phys.* **1944**, *15* (24), 42105–42353.

(24)   Bankoff, S. Ebullition from Solid Surfaces in the Absence of a Pre-Existing Gaseous Phase. *Trans. Am. Sco. Mech. Eng.* **1957**, *79*, 735–740.

(25)   Jones, S. The Cycle of Bubble Production from a Gas Cavity in a Supersaturated Solution. *Adv. Colloid Interface Sci.* **1999**, *80* (1), 51–84.

(26)   Huang, W.; Manjare, M.; Zhao, Y. Catalytic Nanoshell Micromotors. *J. Phys. Chem. C* **2013**, *117* (41), 21590–21596.

(27)   Zhou, W.; Wu, X. J.; Cao, X.; Huang, X.; Tan, C.; Tian, J.; Liu, H.; Wang, J.; Zhang, H. Ni_3S_2 Nanorods/Ni Foam Composite Electrode with Low Overpotential for Electrocatalytic Oxygen Evolution. *Energy Environ. Sci.* **2013**, *6* (10), 2921–2924.

(28)   van Drunen, J.; Kinkead, B.; Wang, M. C. P.; Sourty, E.; Gates, B. D.; Jerkiewicz, G. Comprehensive Structural, Surface-Chemical and Electrochemical Characterization of Nickel-Based Metallic Foams. *ACS Appl. Mater. Interfaces* **2013**, *5* (14), 6712–6722.

(29)   Moon, G. D.; Lee, T. I; Kim, B.; Chae, G.; Kim, J.; Kim, S.; Myoung, J. M.; Jeong, U. Assembled Monolayers of Hydrophilic Particles on Water Surfaces. *ACS Nano* **2011**, *5* (11), 8600–8612.

(30)   Kinkead, B.; van Drunen, J.; Paul, M. T. Y.; Dowling, K.; Jerkiewicz, G.; Gates, B. D. Platinum Ordered Porous Electrodes: Developing a Platform for Fundamental Electrochemical Characterization. *Electrocatalysis* **2013**, *4* (3), 179–186.

(31)   Zach, M. P.; Penner, R. M. Nanocrystalline Nickel Nanoparticles. *Adv. Mater.* **2000**, *12* (12), 878–883.

(32)   Alsabet, M.; Grden, M.; Jerkiewicz, G. Electrochemical Growth of Surface Oxides on Nickel. Part

3: Formation of β-NiOOH in Relation to the Polarization Potential, Polarization Time, and Temperature. *Electrocatalysis* **2015**, *6* (1), 60–71.

(33)   van Drunen, J.; Barbosa, A. F. B.; Tremiliosi-Filho, G. The Formation of Surface Oxides on Nickel in Oxalate-Containing Alkaline Media. *Electrocatalysis* **2015**, *6* (5), 481–491.

(34)   Lyons, M. E. G.; Russell, L.; O'Brien, M.; Doyle, R. L.; Godwin, I.; Brandon, M. P. Redox Switching and Oxygen Evolution at Hydrous Oxyhydroxide Modified Nickel Electrodes in Aqueous Alkaline Solution: Effect of Hydrous Oxide Thickness and Base Concentration. *Int. J. Electrochem. Sci.* **2012**, *7* (4), 2710–2763.

(35)   French, H. M.; Henderson, M. J.; Hillman, A. R.; Vieil, E. Ion and Solvent Transfer Discrimination at a Nickel Hydroxide Film Exposed to LiOH by Combined Electrochemical Quartz Crystal Microbalance (EQCM) and Probe Beam Deflection (PBD) Techniques. *J. Electroanal. Chem.* **2001**, *500* (1–2), 192–207.

(36)   Gonsalves, M.; Hillman, A. R. Effect of Time Scale on Redox-Driven Ion and Solvent Transfers at Nickel Hydroxide Films in Aqueous Lithium Hydroxide Solutions. *J. Electroanal. Chem.* **1998**, *454* (1–2), 183–202.

(37)   Hall, D. S.; Bock, C.; MacDougall, B. R. An Oxalate Method for Measuring the Surface Area of Nickel Electrodes. *J. Electrochem. Soc.* **2014**, *161* (12), H787–H795.

(38)   Gong, M.; Dai, H. A Mini Review of NiFe-Based Materials as Highly Active Oxygen Evolution Reaction Electrocatalysts. *Nano Res.* **2014**, *8* (1), 23–39.

(39)   Martin, E. T.; McGuire, C. M.; Mubarak, M. S.; Peters, D. G. Electroreductive Remediation of Halogenated Environmental Pollutants. *Chem. Rev.* **2016**, *116* (24), 15198–15234.

(40)   Hauch, A.; Georg, A. Diffusion in the Electrolyte and Charge-Transfer Reaction at the Platinum Electrode in Dye-Sensitized Solar Cells. *Electrochim. Acta* **2001**, *46* (22), 3457–3466.

(41)   Nicholson, R. S. Theory and Application of Cyclic Voltammetry for Measurement of Electrode Reaction Kinetics. *Anal. Chem.* **1965**, *37* (11), 1351–1355.

(42)   Wipf, D. O.; Kristensen, E. W.; Deakin, M. R.; Wightman, R. M. Fast-Scan Cyclic Voltammetry as a Method to Measure Rapid Heterogeneous Electron-Transfer Kinetics. *Anal. Chem.* **1988**, *60* (4), 306–310.

(43)   Klaus, S.; Cai, Y.; Louie, M. W.; Trotochaud, L.; Bell, A. T. Effects of Fe Electrolyte Impurities on Ni(OH)$_2$/NiOOH Structure and Oxygen Evolution Activity. *J. Phys. Chem. C* **2015**, *119* (13), 7243–7254.

(44)   Boubatra, M.; Azizi, A.; Schmerber, G.; Dinia, A. The Influence of pH Electrolyte on the Electrochemical Deposition and Properties of Nickel Thin Films. *Ionics* **2012**, *18* (4), 425–432.

(45)   Williams, V. O.; Demarco, E. J.; Katz, M. J.; Libera, J. A.; Riha, S. C.; Kim, D. W.; Avila, J. R.; Martinson, A. B. F.; Elam, J. W.; Pellin, M. J.; Farha, O. K. Fabrication of Transparent-Conducting-Oxide-Coated Inverse Opals as Mesostructured Architectures for Electrocatalysis Applications: A Case Study with NiO. *ACS Appl. Mater. Interfaces* **2014**, *6* (15), 12290–12294.

(46)   Gupta, V.; Gupta, S.; Miura, N. Potentiostatically Deposited Nanostructured Co$_x$Ni$_{1-X}$ Layered Double Hydroxides as Electrode Materials for Redox-Supercapacitors. *J. Power Sources* **2008**, *175* (1), 680–685.

(47)   Wang, Y. M.; Zhao, D. D.; Zhao, Y. Q.; Xu, C. L.; Li, H. L. Effect of Electrodeposition

Temperature on the Electrochemical Performance of a Ni(OH)$_2$ Electrode. *RSC Adv.* **2012**, *2* (3), 1074–1082.

(48) Delahaye-Vidal, A.; Figlarz, M. Textural and Structural Studies on Nickel Hydroxide Electrodes. II. Turbostratic Nickel (II) Hydroxide Submitted to Electrochemical Redox Cycling. *J. Appl. Electrochem.* **1987**, *17* (3), 589–599.

(49) Lyons, M. E. G.; Doyle, R. L.; Fernandez, D.; Godwin, I. J.; Browne, M. P.; Rovetta, A. The Mechanism and Kinetics of Electrochemical Water Oxidation at Oxidized Metal and Metal Oxide Electrodes. Part 1. General Considerations: A Mini Review. *Electrochem. commun.* **2014**, *45*, 60–62.

(50) Biesinger, M. C.; Payne, B. P.; Hart, B. R.; Grosvenor, A. P.; McIntryre, N. S.; Lau, L. W.; Smart, R. S. Quantitative Chemical State XPS Analysis of First Row Transition Metals, Oxides and Hydroxides. *J. Phys. Conf. Ser.* **2008**, *100* (1), 1–4.

(51) Burke, M. S.; Enman, L. J.; Batchellor, A. S.; Zou, S.; Boettcher, S. W. Oxygen Evolution Reaction Electrocatalysis on Transition Metal Oxides and (Oxy) Hydroxides: Activity Trends and Design Principles. *Chem. Mater.* **2015**, *27* (22), 7549–7558.

(52) Enman, L. J.; Burke, M. S.; Batchellor, A. S.; Boettcher, S. W. Effects of Intentionally Incorporated Metal Cations on the Oxygen Evolution Electrocatalytic Activity of Nickel (Oxy) Hydroxide in Alkaline Media. *ACS Catal.* **2016**, *6* (4), 2416–2423.

(53) Haasch, R. T. *X-Ray Photoelectron Spectroscopy (XPS) and Auger Electron Spectroscopy (AES)*; Springer: New York, 2014; pp 93–132.

(54) Kim, K. J.; Unger, W. E. S.; Kim, J. W.; Moon, D. W.; Gross, T.; Hodoroaba, V. D.; Schmidt, D.; Wirth, T.; Jordaan, W.; Van Staden, M.; Prins S. Inter-Laboratory Comparison: Quantitative Surface Analysis of Thin Fe-Ni Alloy Films. *Surf. Interface Anal.* **2012**, *44* (2), 192–199.

(55) Kim, K. J.; Moon, D. W.; Park, C. J.; Simons, D.; Gillen, G.; Jin, H.; Kang, H. J. Quantitative Surface Analysis of Fe-Ni Alloy Films by XPS, AES, and SIMS. *Surf. Interface Anal.* **2007**, *39* (8), 665–673.

(56) Nydegger, M. W.; Couderc, G.; Langell, M. A. Surface Composition of Co$_x$Ni$_{1-x}$O Solid Solutions by X-Ray Photoelectron and Auger Spectroscopies. *Appl. Surf. Sci.* **1999**, *147* (1), 58–66.

(57) Chang, Y.; Feng, S. Stepwise Anodic Electrodeposition of Nanoporous NiOOH/Ni(OH)$_2$ with Controllable Wettability and Its Applications. *HKIE Trans.* **2015**, *22* (4), 202–211.

(58) Lv, S.; Suo, H.; Wang, J.; Wang, Y.; Zhao, C.; Xing, S. Facile Synthesis of Nanostructured Ni(OH)$_2$ on Nickel Foam and Its Electrochemical Property. *Colloids Surfaces A Physicochem. Eng. Asp.* **2012**, *396*, 292–298.

(59) Chen, L.; Du, Y.; Huang, Y.; Ng, P. F.; Fei, B. Facile Fabrication of Hierarchically Structured PBO-Ni(OH)$_2$/NiOOH Fibers for Enhancing Interfacial Strength in PBO Fiber/epoxy Resin Composites. *Compos. Sci. Technol.* **2016**, *129*, 86–92.

(60) Cassie, B D; Baxter, S. Wettability of Porous Surfaces. *J. Chem. Soc, Farraday Trans.* **1944**, *5*, 546–551.

(61) Erbil, H. Y.; Cansoy, C. E. Range of Applicability of the Wenzel and Cassie-Baxter Equations for Superhydrophobic Surfaces. *Langmuir* **2009**, *25* (24), 14135–14145.

(62) Li, J.; Cheng, H. M.; Chan, C. Y.; Ng, P. F.; Chen, L.; Fei, B.; Xin, J. H. Superhydrophilic and

Underwater Superoleophobic Mesh Coating for Efficient Oil–water Separation. *RSC Adv.* **2015**, *5* (64), 51537–51541.

(63)   Bard, A. J.; Faulkner, L. R. *Electrochemical Methods:Fundamentals and Applications*, 2nd Ed.; John Wiley & Sons, Inc.: New York, NY, 2015; Vol. 8, pp 129–133.

(64)   Kadyk, T.; Bruce, D.; Eikerling, M. How to Enhance Gas Removal from Porous Electrodes? *Sci. Rep.* **2016**, *6*, 1–14.

(65)   Vogt, H.; Stephan, K. Local Microprocesses at Gas-Evolving Electrodes and Their Influence on Mass Transfer. *Electrochim. Acta* **2015**, *155*, 348–356.

(66)   Chen, Q.; Luo, L.; White, H. S. Electrochemical Generation of a Hydrogen Bubble at a Recessed Platinum Nanopore Electrode. *Langmuir* **2015**, *31* (15), 4573–4581.

(67)   Li, F. B.; Lubetkin, S. D.; Roberts, D. J.; Hillman, A. R. Electrogravimetric and Chronoamperometric Monitoring of Individual Events of Growth and Detachment of Electrolytic Chlorine Gas Bubbles. *J. Chem. Soc. Chem. Commun.* **1994**, *180* (2), 159–160.

(68)   Balzer, R. J.; Vogt, H. Effect of Electrolyte Flow on the Bubble Coverage of Vertical Gas-Evolving Electrodes. *J. Electrochem. Soc.* **2003**, *150* (1), E11–E16.

(69)   Choi, C.; David, M.; Gao, Z.; Chang, A.; Allen, M.; Wang, H. Large-Scale Generation of Patterned Bubble Arrays on Printed Bi-Functional Boiling Surfaces. *Sci. Rep.* **2016**, *6*, 1–10.

(70)   Zhang, D.; Zeng, K. Evaluating the Behavior of Electrolytic Gas Bubbles and Their Effect on the Cell Voltage in Alkaline Water Electrolysis. *Ind. Eng. Chem. Res.* **2012**, *51* (42), 13825–13832.

TOC Graphic

$$4OH^- \rightarrow O_2 + 2H_2O + 4e^-$$